Energy & Environmental Science

ROYAL SOCIETY OF CHEMISTRY

PAPER

View Article Online
View Journal | View Issue

Check for updates

Cite this: *Energy Environ. Sci.*, 2022, **15**, 2021

Membrane-less amphoteric decoupled water electrolysis using WO_3 and $Ni(OH)_2$ auxiliary electrodes†

Martins Vanags,[a] Guntis Kulikovskis,[a] Juris Kostjukovs,[b] Laimonis Jekabsons,[c] Anatolijs Sarakovskis,[c] Krisjanis Smits,[c] Liga Bikse[c] and Andris Šutka *[a]

Energy storage and delivery play a crucial role in the effective management of renewable power sources such as solar and wind. Hydrogen energy is proposed to be one of the major substitutes to fill the gap between the production plant and consumer. The energy from renewable power sources is used to generate hydrogen, which is later converted to electricity and water. Hydrogen generation in water electrolysis from renewable energy is a sustainable process. However, the need for membrane separation of hydrogen from oxygen in single-cell water electrolysis is detrimental. Moreover, the hydrogen production rate in conventional single-cell electrolysers is strictly limited by the rate of oxygen evolution. Recently decoupled water electrolysis has been proposed where hydrogen and oxygen are generated in spatially separated alkaline cells. Here we demonstrate amphoteric decoupled electrolysis by using an auxiliary electrode (AE) couple with H_xWO_3 and NiOOH being employed in separate acid and alkaline cells, respectively. The average electrolysis efficiency of the proposed concept is up to 71%, higher than that observed from decoupled electrolysis where both cells are alkaline.

Received 23rd December 2021,
Accepted 7th March 2022

DOI: 10.1039/d1ee03982b

rsc.li/ees

Open Access Article. Published on 05 April 2022. Downloaded on 8/20/2025 12:00:37 PM.
This article is licensed under a Creative Commons Attribution 3.0 Unported Licence.

Broader context

Hydrogen is a road to clean and secure energy. Hydrogen has the highest gravimetric energy density and can be used in fuel cells, internal combustion engines, and other energy generating units producing only clean water in the exhaust. Hydrogen is not available in free form on our planet and therefore it needs to be produced from water by electrolysis, which is also a perfect solution for the management of power sources such as solar or wind. In conventional single-cell electrolysers, however, the cathode must be separated from the anode by a diaphragm or membrane to avoid the formation of an explosive gas mixture. Both the diaphragm and membrane have an ion diffusion resistance that increases the reaction overpotential and has a direct effect on efficiency. The decoupled electrolysis strategy implemented in 2017 with solid $Ni(OH)_2$ and NiO(OH) auxiliary electrodes (ref. 22) avoids using a membrane and mixing of gases because the cathode is spatially separated from the anode in two individual cells. Here we present amphoteric decoupled electrolysis by using WO_3 and $Ni(OH)_2$ auxiliary electrodes, thus providing a high energy efficiency of 74%.

Introduction

With the increase of energy production from renewable sources (wind energy, solar energy, hydropower, *etc.*), there is an emerging need for efficient energy storage. A grid-connected system is used to transform the produced energy to be fed into the central electricity grid. However, this approach suffers from overgeneration, and variable load patterns generated by renewable energy plants.[1] Due to this reason energy storage is becoming one of the main priorities. The conventional technologies for energy storage such as water pumping and air compression are being replaced by alternative technologies, for example, electrochemical batteries that are being used on a large scale.[2,3] However, in many cases the energy efficiency of batteries is below 50%.[4] For Li-ion batteries efficiency as high as 83% has been reported.[2] However, Li is expensive and a scarce material with a potential supply risk.[5]

The other option is to use an energy carrier such as hydrogen. Hydrogen has a high gravimetric energy density of 33.3 kW h kg^{-1} and it can be converted into electricity using an internal combustion engine or fuel cells with the production of

[a] *Institute of Materials and Surface Engineering, Faculty of Materials Science and Applied Chemistry, Riga Technical University, P. Valdena Street 3, Riga LV1048, Latvia. E-mail: andris.sutka@rtu.lv*
[b] *Department of Physical Chemistry, University of Latvia, LV1004 Jelgavas Street 1, Riga, Latvia*
[c] *Institute of Solid State Physics, University of Latvia, Kengaraga Street 8, Riga LV1063, Latvia*

† Electronic supplementary information (ESI) available. See DOI: 10.1039/d1ee03982b

Open Access Article. Published on 05 April 2022. Downloaded on 8/20/2025 12:00:37 PM.
This article is licensed under a Creative Commons Attribution 3.0 Unported Licence.

water as the only by-product.[6] Hydrogen can also be used in syngas for the Fischer–Tropsch synthesis of lower olefins, gasoline, diesel, and jet fuel by the transformation of nonpetroleum carbon resources.[7]

Water electrolysis in conjunction with renewable energy sources such as solar or wind is an environmentally friendly path for hydrogen production. The energy efficiency of electrolysis is determined by the ratio between the produced hydrogen and electrical energy consumed. For water electrolysis, there are two commercialized technologies available, alkaline electrolysers and proton exchange membrane (PEM) electrolysers. A proton exchange membrane (PEM) or a diaphragm (alkaline medium) is used to separate H_2/O_2 and avoid the formation of an explosive gas mixture. Acid PEM electrolysers are constructed from proton exchange membranes and expensive catalysts like Pt and Ir.[8] Alkaline electrolysers use cheaper catalysts like Ni and exhibit long-term operation.[9] The stack efficiency for both, alkaline and PEM electrolysers, is 70%.[10]

Membrane/diaphragm-based electrolysers have several limitations: (i) unbalanced pressure in two sides (ii) high ion diffusion resistance and (iii) high cost. The membrane/diaphragm undergoes continuous deformation because the released hydrogen volume is twice as much as oxygen volume leading to membrane failure. Also, the membrane/diaphragm has an ion diffusion resistance that increases the reaction overpotential and has a direct effect on the efficiency. Thicker membranes have a longer lifetime (mechanical and chemical durability), but the overall efficiency of the electrolyser is reduced due to increased overvoltage. Conventional water electrolysis is usually conducted with a large voltage input of 1.8–2.4 V.[11]

The thermodynamic efficiency limit of water electrolysis is determined by the sum of hydrogen evolution reaction (HER) and oxygen evolution reaction (OER) standard potentials (1.23 V). The standard potential of the HER at pH 0 is 0 V *vs.* the standard hydrogen electrode (SHE) and the standard potential of the OER is +1.23 V. In an alkaline medium, the standard potential for the oxygen evolution reaction at pH 14 is +0.4 V against the SHE and the standard potential for the HER is −0.83 V.[12] If the HER was realized in an acidic environment and the OER in an alkaline environment (amphoteric electrolysis), then the water splitting standard potential would be only 0.4 V. It has been demonstrated that the energy required for water splitting can be greatly reduced by combining acidic and alkaline electrolytes for the HER and OER, respectively.[13–16] By using a bipolar membrane for ion conduction and acid-alkaline separation into one single electrolyser, water amphoteric electrolysis has been driven by applied voltages as low as 1.2 V at 40 mA cm^{-2},[13] 0.84 V at 13 mA cm^{-2},[15] and 0.79 V at 10 mA cm^{-2}.[15] The energy consumption for hydrogen production was reduced by 30–35%. The main drawback of the amphoteric electrolysis concepts proposed so far is the need for costly bipolar membranes.

Redox mediator assisted electrolysis has been demonstrated in the literature to decouple the HER from the OER and avoid membranes. First, the mediator is protonated and then converted back to its initial form. The step of deprotonation has been realized over a special catalyst or by connecting to another working electrode.[17–21] However, H_2 and O_2 in redox couple mediated water electrolysis are produced in separate steps thus making the process time-consuming and complicated to perform.

Recently, the simultaneous generation of H_2 and O_2 in separate cells has been demonstrated by using an auxiliary electrode (AE) couple – NiOOH and $Ni(OH)_2$.[22] In the proposed decoupled electrolysis the water is reduced in the cathode cell as follows: $4H_2O + 4e^- \rightarrow 2H_2 + 4OH^-$. Hydroxyl ions are further consumed by the $Ni(OH)_2$ AE that transforms into NiOOH as follows: $Ni(OH)_2 + OH^- - e^- \rightarrow NiOOH + H_2O$. In the anode cell, the OER occurs according to the equation: $4OH^- \rightarrow O_2 + 2H_2O + 4e^-$, where OH^- is supplied by the AE: $NiOOH + H_2O + e^- \rightarrow Ni(OH)_2 + OH^-$. This electrolysis process is driven by a very high average electrolysis efficiency of 58%. However, both spatially separated cells in the proposed electrolyser are alkaline. Here we show that the electrolysis efficiency of this concept can be readily enhanced by combining an acid and alkaline cell. Herein we demonstrate for the first time a membrane-less decoupled amphoteric electrolyser where the alkaline and acid cells are spatially separated by using WO_3 and $Ni(OH)_2$ auxiliary electrodes.

Results and discussion

Amphoteric decoupled water splitting was realized on an electrolyser (Fig. 1) constructed from two separate cells filled with 0.5 M H_2SO_4 and 1 M KOH aqueous solutions. Two primary Pt electrodes were placed in separate cells – the cathode in an acid cell and the anode in an alkaline cell for realizing the HER or OER. WO_3 and $Ni(OH)_2$ were used as auxiliary electrode materials to operate in acidic and basic media, respectively. WO_3 nanoparticles in the diameter range of 30–70 nm, as estimated from SEM studies (ESI,† Fig. S1), were synthesized by a hydrothermal method. The prepared WO_3 nanoparticles consist of a single tungsten oxide hydrate phase as demonstrated by XRD studies (ESI,† Fig. S2). The layered structure of tungsten oxide hydroxide has shown a better capacity for the insertion of cations.[23] The β-$Ni(OH)_2$ nanoparticles (diameter ∼18 nm) were used as received from the supplier. For the preparation of the AEs, WO_3 nanoparticles were deposited on Ti foam and β-$Ni(OH)_2$ nanoparticles were deposited on the porous Ni mesh. All details related to the materials synthesis and preparation are given in the Experimental section. The electrochemical properties of the WO_3 and $Ni(OH)_2$ electrodes are discussed in detail in the ESI† (section S2, Fig. S3, S4 and Tables S1, S2).

During electrolysis, an external power source was employed to power the primary Pt anode and Pt cathode. The reactions occurring on the primary and auxiliary electrodes depend on the polarity of the applied potential. At the first cycle, during the water splitting, the tungsten oxide is protonated to tungsten bronze ($WO_3 + xe^- + xH^+ \rightarrow H_xWO_3$) and nickel hydroxide is

 This journal is © The Royal Society of Chemistry 2022

Open Access Article. Published on 05 April 2022. Downloaded on 8/20/2025 12:00:37 PM.
This article is licensed under a Creative Commons Attribution 3.0 Unported Licence.

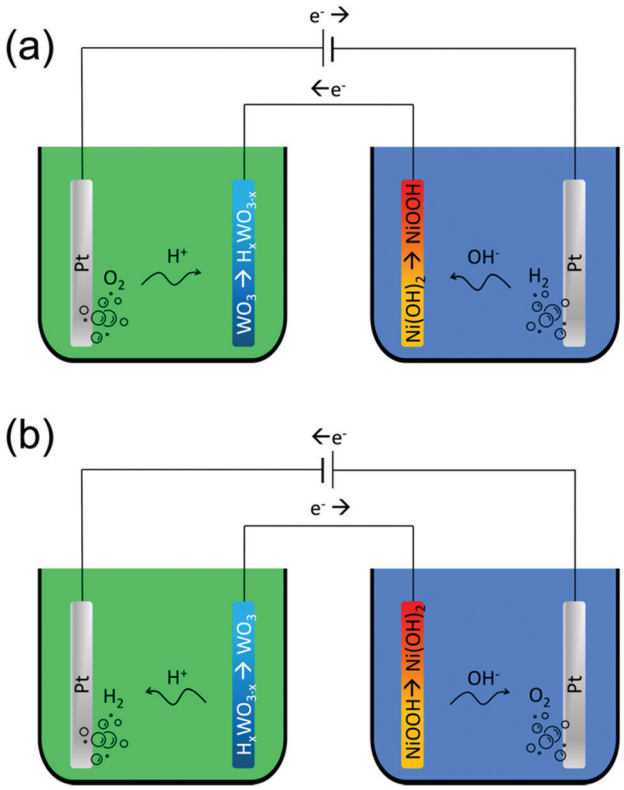

Fig. 1 The scheme of the spatially decoupled amphoteric water electrolyser operating in two different modes with different polarities of the applied potential. The green cell represents the acid environment and the blue cell represents the alkaline environment. Water splitting is observed at the first step (a) while at the second (favourable) step (b) the gases are generated under low potential from ions provided by AEs.

transformed into nickel oxyhydroxide ($Ni(OH)_2 + OH^- \rightarrow NiOOH + e^- + H_2O$). As discussed below, this step is energetically costly because the OER occurs on Pt in the acidic cell ($2H_2O \rightarrow O_2 + 4e^- + 4H^+$) while the HER ($2H_2O + 2e^- \rightarrow H_2 + 2OH^-$) occurs in the alkaline cell.

In the case of electron flow from the Pt anode to cathode, the HER ($2H^+ + 2e^- \rightarrow H_2$) occurs on the cathode in the acidic cell. H^+ ions are provided by the H_xWO_3 auxiliary electrode. During the H^+ conversion to H_2 gas, H_xWO_3 transforms into WO_3. Simultaneously, the OER occurs on the anode in the alkaline cell ($4OH^- \rightarrow O_2 + 2H_2O + 4e^-$), converting OH^- ions supplied by the NiOOH auxiliary electrode to O_2 and H_2O. During the OER the NiOOH is transformed into $Ni(OH)_2$ after the reaction: $NiOOH + e^- + H_2O \rightarrow Ni(OH)_2 + OH^-$. The OER and HER proceed in this direction until the H_xWO_3 is converted to WO_3 and the NiOOH is converted to $Ni(OH)_2$. Since the gases are generated from ions provided by AEs, and the HER occurs in the acid media and the OER occurs in the alkaline media, the hydrogen generation at the second (favourable) step is highly beneficial as discussed below.

One of the preconditions for the AEs to be used in decoupled amphoteric electrolysis is that their reduction and oxidation must occur between the OER and HER onset potentials. To qualitatively determine the electrochemical profiles of WO_3 and

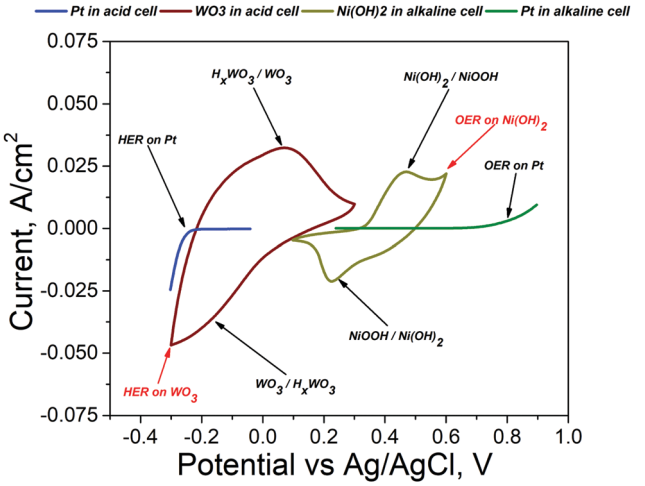

Fig. 2 Location of oxidation and reduction peaks of redox mediator electrodes between the OER and HER onset potentials.

$Ni(OH)_2$, cyclic voltammetry (CV) studies were performed for both electrode materials in a typical three-electrode system using Pt as the counter electrode and Ag/AgCl as the reference electrode. CV measurements were used to also determine the onset potentials of the HER and OER for platinum. An aqueous 0.5 M H_2SO_4 electrolyte was used in the case of WO_3, but 1 M NaOH electrolyte was used in the case of $Ni(OH)_2$.

The deintercalation of H^+ from H_xWO_3 (brown curve maximum at 0.071 V on Fig. 2) is 0.3 V above the HER onset potential (blue curve at −0.235 V). The NiOOH reduction minimum (dark yellow curve minimum at 0.226 V) is 0.57 V below the OER onset potential (green curve at 0.8 V). The onset potential for H^+ intercalation in WO_3 in the acid cell is 0 V and saturation of the curve is reached at −0.2 V which is 0.1 V above the HER onset potential. The oxidation maximum potential of NiOOH to $Ni(OH)_2$ in the alkaline cell is 0.467 V which is 0.11 V below the OER onset potential. The HER on the WO_3 electrode in the acid cell and the OER on the $Ni(OH)_2$ electrode in the alkaline cell are close to the WO_3 intercalation reaction and $Ni(OH)_2$ oxidation potential, respectively (Fig. 2 shows both reactions in red). The proximity of the OER and HER imposes criteria to carefully select a potential window for the operation of the amphoteric electrolyser.

The reduction and oxidation of WO_3 and $Ni(OH)_2$ electrodes was followed by XPS. The samples were oxidised and reduced at potentials that allow avoiding the HER on OER on AEs. The spectra of W and Ni recorded for WO_3 before and after the H^+ intercalation and for oxidized and reduced $Ni(OH)_2$ are shown in Fig. 3. The spectrum of W of the WO_3 electrode consists of peaks of binding energy at 35.8 eV ($4f_{7/2}$), 38.0 eV ($4f_{5/2}$), and 41.6 eV (loss feature of W). Similar values have been reported in ref. 23 for WO_3 (Fig. 3a). The spectrum of tungsten bronze contains additional peaks at 34.4 eV ($4f_{7/2}$) and 36.4 eV ($4f_{5/2}$). The respective peaks are located at lower binding energies implying that the additional features correspond to tungsten in a lower oxidation state (Fig. 3b).

Open Access Article. Published on 05 April 2022. Downloaded on 8/20/2025 12:00:37 PM.
This article is licensed under a Creative Commons Attribution 3.0 Unported Licence.

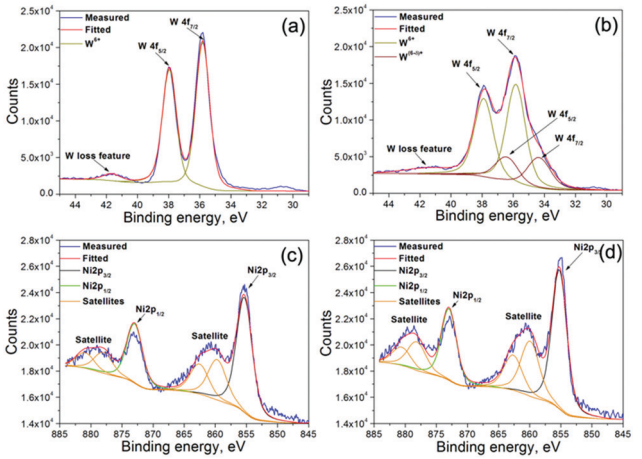

Fig. 3 XPS spectra of (a) deintercalated WO_3, (b) intercalated WO_3, (c) reduced $Ni(OH)_2$ and (d) oxidized $Ni(OH)_2$ samples.

The binding energies of the peaks corresponding to Ni $2p_{3/2}$ and Ni $2p_{1/2}$ in the nickel hydroxide electrode are observed at 855.2 eV and 873.0 eV, respectively. Additional peaks (859.9 eV, 862.7 eV, and 878.1 eV, and 880.6 eV), which are present in the vicinity of the main peaks, are identified as the satellites (Fig. 3c). The binding energies of the observed peaks are similar to the ones reported for $Ni(OH)_2$.[24] The respective peaks measured for the nickel oxyhydroxide appear at 855.2 eV and 873.0 eV ($2p_{3/2}$ and $2p_{1/2}$) with the satellites at 859.7 eV, 862.5 eV, 878.0 eV and 880.9 eV (Fig. 3d). One can see that the positions of the peaks do not change upon electrochemical oxidation. This fact combined with the XRD measured for the oxidized nickel hydroxide electrode suggests the formation of β-NiOOH.[24]

The chronopotentiometry measurements were performed under constant 10 mA current between the Pt anode and cathode to demonstrate the stability of the proposed electrolysis device, as well as to determine the potential window between the electrolysis modes, where the favourable direction represents the simultaneous OER and HER in the alkaline and acid cells from ions provided by AEs. To suppress the OER and HER on the auxiliary electrodes, the threshold potential in the favourable direction was set to 1 V, while the unfavourable reaction threshold was set to −3.5 V.

The chronopotentiometry curve showing potential *versus* time for 10 cycles is demonstrated in Fig. 4a. As expected, the cell operates asymmetrically. In the favourable direction, the applied potential of 0.68 V is needed to afford 10 mA current. It is a lower value when compared to that reported previously using bipolar membranes for amphoteric electrolysis (0.79 V)[14] indicating a smaller overpotential on the auxiliary electrodes compared to the membrane. In the opposite direction −2.93 V is necessary to afford 10 mA current. A large potential is needed to operate the OER in the acidic environment and the HER in the alkaline environment. The specific capacity of AEs in chronopotentiometry measurements is 55 mA h g^{-1}. The total specific capacity observed from CV measurements for the

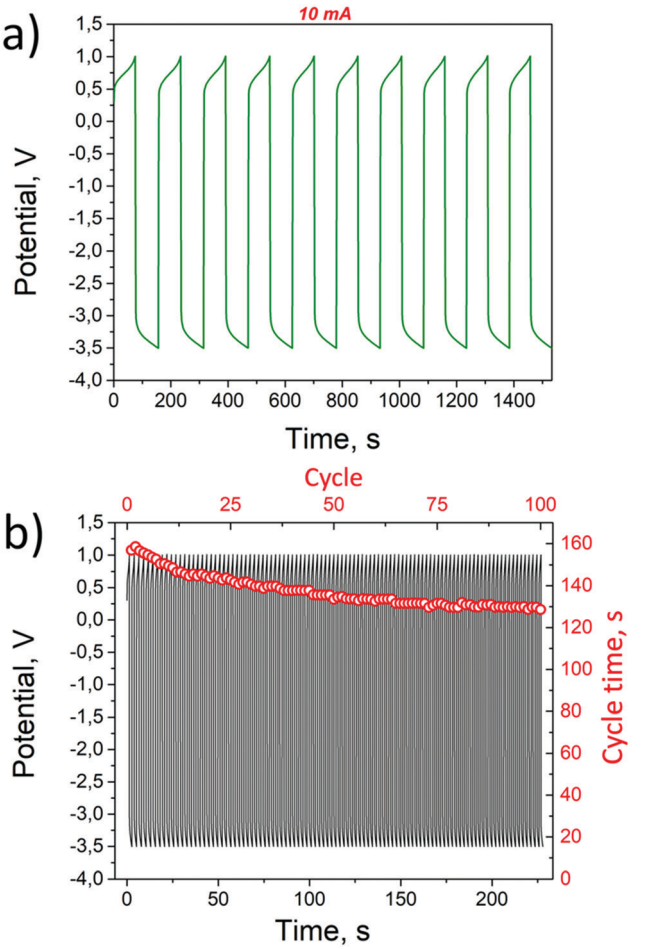

Fig. 4 Chronopotentiometry measurements for 10 cycles (a) and for 100 cycles (b) demonstrating stability.

$Ni(OH)_2$ electrode was 78 mA h g^{-1} and −96 mA h g^{-1} for WO_3 (ESI,† section S2). Thus the percentage of the AE material that has undergone reaction from chronopotentiometry measurements is 70.5%. The smaller specific capacity in chronopotentiometry measurement can be explained by a major structural change in the intercalation material[2] and the high current/active substance ratio.[25]

The shape of the voltage curve in the two directions is also different. In the favourable direction, the voltage curve bends up rapidly at the end of the cycle indicating the complete conversion of the auxiliary electrodes. In the other direction where $Ni(OH)_2$ is transformed into NiOOH but WO_3 to H_xWO_3, the applied voltage at the end of the cycle does not exhibit a sudden increase. It was observed that the slope decreases to the threshold −3.5 V but no saturation is obtained. This behaviour indicates that the HER on the WO_3 auxiliary electrode is close to the applied potential for the HER on WO_3 as demonstrated by the CV measurements above (Fig. 2). However, the duration of each half-cycle does not change more than 0.25% at each step. This indicates that there is a complete switching between the two chemical states of AEs during the operation and the voltage window has been selected correctly. The time for the

 This journal is © The Royal Society of Chemistry 2022

Open Access Article. Published on 05 April 2022. Downloaded on 8/20/2025 12:00:37 PM.
This article is licensed under a Creative Commons Attribution 3.0 Unported Licence.

full cycle drops by about ~25% in 100 steps as demonstrated in Fig. 4b.

Both qualitative and quantitative gas analyses were performed. The qualitative analysis aimed to find out the purity of the gases during each cycle in the acid and alkaline cells. Gas purity from each cell was analysed by mass spectrometry (MS) by using a specially designed custom-made cell (ESI,† Fig. S5). The cell was operated at a threshold potential to avoid the HER or OER on AEs (experimental details can be found in ESI,† section S3). In the acid cell, in the favourable operation regime, the H_2 concentration was 99.6% and the oxygen concentration was 0.4%, while in the alkaline cell the O_2 concentration was 99.6% and the H_2 concentration was 0.4%. The mass spectra and gas concentration values are presented in ESI,† section S3, Fig. S6–S9 and Table S3. In the other operation regime, the gas composition was opposite as expected. The O_2 concentration in the acid cell was 99.7% and the H_2 concentration was 0.3%, while in the alkaline cell, the H_2 concentration was 99.8% and the O_2 concentration was 0.2%.

The volume of hydrogen, produced during the two different operation regimes, was measured to determine the current efficiency (faradaic efficiency). The volume measurement of the produced hydrogen was carried out with the volumetric displacement method. The hydrogen volume was measured in an acid cell during a favourable cycle and in an alkaline cell during an unfavourable cycle. A glass capillary with an inner diameter of 1 mm was used as a displacement volume (ESI,† section S4 and Fig. S10). Knowing the produced hydrogen gas volume V, the electrolysis current I, and the cycle time t, the current efficiency was calculated according to the formula:

$$\eta_F = \frac{kVF}{22.4It} \quad (1)$$

where 22.4 L mol^{-1} is the volumetric Avogadro number, F is the Faraday constant, and $k = 2$ in the HER. The faradaic efficiency in both operation regimes was found to be 98% (ESI,† section S4 and Tables S5, S6).

Energy efficiency was calculated separately for the two regimes, as well as for the whole operation cycle based on Faraday's efficiency value. The consumed electrical energy is equal to:

$$E = I\int \nu(t)\mathrm{d}t \quad (2)$$

where E is the electrical energy consumed, I is the current during the cycle and the integral is the area under the potential curve obtained from chronopotentiometry.

The energy that can be obtained from the hydrogen gas produced using the highest heating value HHV is:

$$E_H = \frac{\eta_F It M_{mol} \mathrm{HHV}}{F} \quad (3)$$

where M_{mol} is the molar mass of H (0.001 kg mol^{-1}), HHV is the highest heating value for hydrogen gas (140 MJ kg^{-1}) and F is the Faraday constant. The factor η_F is faradaic efficiency 0.98.

The efficiency is obtained by dividing E_H by E and combining the eqn (2) and (3) gives an expression for determining the efficiency:

$$E_H = \frac{\eta_F t M_{mol} \mathrm{HHV}}{F\int \nu(t)\mathrm{d}t} \quad (4)$$

In the favourable regime, the value of the energy efficiency coefficient is 201%, while during the reverse half-cycle the value is 43%. The overall cycle has an energy efficiency of 71%. It is 13% higher than the efficiency reported previously for a decoupled electrolysis device using $Ni(OH)_2$ AEs.[22]

Although we have demonstrated a promising decoupled amphoteric electrolysis process, it is important to show that the proposed system can operate with higher current density values in the range of 50–100 mA to prove the feasibility of the concept. To perform measurements at 100 mA, AEs with optimised current/mass ratio are needed. To maintain stable operation the current/mass ratio should be 1 A g^{-1} of active substance.[25] To reach the desired mass/current ratio, AEs were prepared by using a carbon mat substrate.

To provide a current density of 100 mA, 1.15 V is required to be applied between the cathode and the anode in the favourable direction, but in the opposite direction, 100 mA current was achieved approximately at −2.4 V potential. The chronopotentiometric curve in the opposite direction in the 100 mA mode changes the slope at −3.2 V, which indicates the start of the unwanted HER and OER on the AEs (ESI,† Section S5 and Fig. S11). When compared with 10 mA measurement (where WO_3 was deposited on a Ti substrate, and $Ni(OH)_2$ on a Ni substrate) the required potential in the favourable direction is larger but in the opposite direction it is smaller. By reducing the electrolysis current from 100 mA to 50 mA and 10 mA, a further voltage drop is observed in the unfavourable direction (ESI,† section S6 and Fig. S12). To provide 50 mA current, the required voltage plateau started at around 2 V, thus increasing the efficiency in the unfavourable direction. At 10 mA, chronopotentiometry is divided into two parts, where the current is initially supplied at a voltage less than the thermodynamic limit (2.03 V, which is formed from the 1.23 V standard potential in the OER acidic environment and the −0.83 V standard potential in the HER alkaline medium). This can be related to ion accumulation on more active sites. Electrochemical intercalation starts at about 2 V, which is in line with thermodynamics.

Experiments show that the potential for ion accumulation in the AEs based on carbon cloth decreases but for release, it increases when compared with WO_3 and NiOOH AEs deposited on Ti and Ni substrates, respectively. The carbon fibre substrate and current appear to play a major role in operating potentials. Sites for ion accumulation into the carbon electrode material seem more accessible. This has been observed also in studies related to batteries. Carbon provides active sites and promotes ion intercalation.[2]

The electrolyser based on carbon cloth substrate AEs operating at 100 mA maintains similar gas purity to the cell operating at 10 mA based on a Ti electrode substrate. In the

Open Access Article. Published on 05 April 2022. Downloaded on 8/20/2025 12:00:37 PM.
This article is licensed under a Creative Commons Attribution 3.0 Unported Licence.

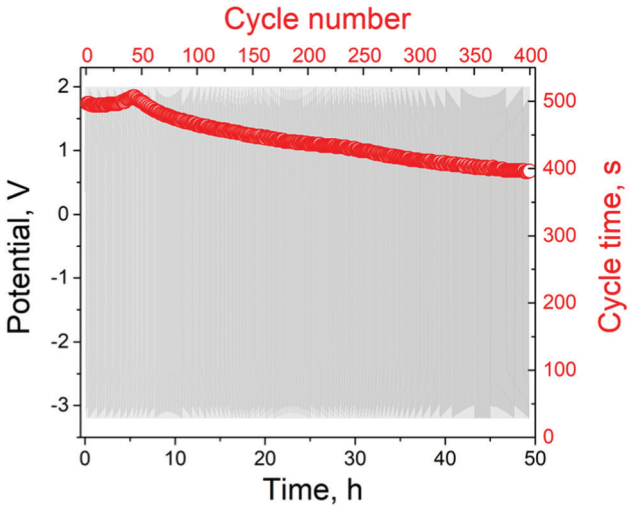

Fig. 5 Chronopotentiometry measurements in 100 mA current mode for the electrolyser operating using AEs on carbon cloth.

favourable regime the H_2 concentration in the acid cell was 99.9% and the oxygen concentration was 0.1%, while in the alkaline cell the O_2 concentration was 99.4% and the H_2 concentration was 0.6%. In the opposite direction the O_2 concentration in the acid cell was 98.8% and the H_2 concentration was 1.2%, while in the alkaline cell the H_2 concentration was 99.5% and the O_2 concentration was 0.5% (ESI,† Section S3, Fig. S7, S8 and Table S4).

The faradaic efficiency for the decoupled amphoteric electrolyser operating at 100 mA was 96–98% (ESI† Tables S7 and S8), but the overall cycle energy efficiency was 67%. The efficiency in the favourable direction was 95%, but in the opposite direction it is 50%. It is worth noting that the full cycle energy efficiency for the electrolyser operating using AEs on the carbon mat substrate was higher on lower currents – 70% at 50 mA and 74% at 10 mA. The efficiency of industrially available alkaline electrolysers is estimated to be around 70%.[2] This efficiency is comparable to that obtained using the decoupled electrolysis concept proposed here.

The electrolyser was operated at 100 mA for 50 hours to demonstrate its stability (Fig. 5). The cycle time decreases only by 21% for 50 h, indicating satisfactory stability of AEs in the amphoteric decoupled electrolyser. In order to better understand the degradation of the AEs, chronopotentiometry measurements for WO_3 and NiOOH were performed in single acid and alkaline cells, respectively. The main indicator of stability in these measurements was the time of the chronopotentiometry cycle, which remained unchanged for 10 hours for the WO_3 electrode. For the $Ni(OH)_2$ electrode the cycle time remained the same only for five hours and then dropped by 30% over the next five hours (ESI,† section S7 and Fig. S13, S14). The β-$Ni(OH)_2$/β-NiOOH redox couple is relatively stable during charge and discharge, but extended charging causes formation of γ-NiOOH, which leads to a deterioration in the electrode performance.[26] At the same time, WO_3 has previously been shown to be stable in sulfuric acid solution both as an energy storage electrode[27] and as a photochromic material.[28]

Conclusions

The novel membrane-less amphoteric decoupled water electrolysis concept has been demonstrated. The electrolyser consists of two spatially separated cells – one acidic and the other alkaline. Separate cells were connected by AEs. WO_3 was used as an AE operating in an acidic cell but $Ni(OH)_2$ was used in an alkaline cell. The potential for gas generation depends on the polarity of the applied potential. Different chemical processes occur at different polarities. In both cycles, hydrogen and oxygen are generated in separate cells. In the first cycle, simultaneous water splitting and ion accumulation in AEs occur. In the second cycle, hydrogen and oxygen are generated in acid and alkaline cells, respectively, from ions released from AEs. The total energy efficiency of the provided electrolysis concept is up to 71%. The energy efficiency is dependent on the operating current and properties of AEs.

Experimental

Material synthesis and electrode preparation

WO_3 nanopowder was prepared by a hydrothermal method based on a procedure published in ref. 27. In a typical synthesis, 0.6 g of $Na_2WO_4{\cdot}2H_2O$ (Sigma Aldrich, 99%) was dissolved in 10 mL of deionized water. After stirring using a magnetic stirrer for 10 min, 2 mL of 3 M HCl solution was added to the solution and stirred continuously for 1 h. By this time the solution had turned to a milky appearance. The mixture was filled into a 50 mL Teflon liner and sealed in a stainless-steel autoclave. The autoclave was heated for 12 h at 160 °C and naturally cooled to room temperature. The resulting precipitate was washed four times with deionized water by centrifugation. The resulting precipitate was dried at 80 °C and then annealed at 270 °C in an air atmosphere for 2 h. After annealing, a yellow WO_3 powder was obtained.

The redox electrode was prepared using a porous titanium substrate (pore size 20–50 μm, porosity 35%, Vector Trading Company). The substrate was cut into 1.5 × 3.5 cm plates and washed in an ultrasonic bath in acetone for 10 min and then in deionized water for an additional 10 min. WO_3, carbon black (CB), and polyvinylidene fluoride (PVDF) were mixed in a weight ratio of 85 : 7.5 : 7.5% according to the following procedure. The WO_3 nanopowder and activated carbon were mixed into a uniform mass by using a mortar pestle and added to PVDF 15% solution in DMF. Stirring for 30 min resulted in a homogeneous slurry. A Ti foam substrate was placed in the slurry and kept in a vacuum desiccator for 30 minutes and then dried at 80 °C for 1 h in an ambient atmosphere. The prepared electrode was then placed in a vacuum oven and kept at 125 °C for 12 h. The mass of WO_3 per 1 cm^2 electrode was about 5 mg.

Ni foam (pore size 50–100 μm, porosity 75–98%, Xiamen Lith Machine Limited) was used as a substrate for $Ni(OH)_2$.

 This journal is © The Royal Society of Chemistry 2022

Open Access Article. Published on 05 April 2022. Downloaded on 8/20/2025 12:00:37 PM.
This article is licensed under a Creative Commons Attribution 3.0 Unported Licence.

It was cut into 1.5 × 3.5 cm plates and washed in acetone and water for 10 min in an ultrasonic bath. β-$Ni(OH)_2$ nanopowders (purity: 99.99%, particle size: 18 nm, Nanografi) were mixed with carbon black and PVDF in a weight ratio of 85 : 7.5 : 7.5% according to the same procedure as in the preparation of the WO_3 electrode.

The electrode for 100 mA measurement was prepared by using untreated carbon fibre cloth (200 g m^{-2}, 0.28 mm thick) as the electrode substrate. The diameter of individual fibres is around 5 μm. The carbon cloth was washed in ethanol and deionized water in an ultrasonic bath for 15 min and dried at 60 °C for 1 hour. Pieces of carbon cloth with an area of 18 cm^2 were assembled in a 4 mm thick laminate with 14 layers. The suspension of $Ni(OH)_2$ or WO_3 nanopowder, PVDF and carbon black in a weight ratio of 85 : 7.5 : 7.5 wt% was prepared. The carbon cloth laminate was dipped into the mixture and impregnated in an ultrasonic bath for 10 min. After impregnation, the electrode material was dried in a vacuum for 12 hours at 125 °C. The mass of the active substance impregnated in the substrate was determined by weighing the carbon cloth before and after impregnation and drying. Assuming that the active substance is homogeneously distributed over the area of the carbon cloth, the mass used in the electrode was determined by cutting the required area.

Material characterization

High-resolution scanning electron microscopy (SEM, Helios 5 UX, ThermoFisher Scientific) was used for sample morphology studies. Powder XRD measurements were performed on a PANalytical X'Pert Pro MRD diffractometer using copper Kα radiation with Bragg–Brentano theta–theta geometry and a PIXcel (1D) detector. The tube voltage and current were set to 40 kV and 30 mA, respectively. The patterns were recorded from 5° to 100° on the 2θ scale, using a scan speed of 0.26° s^{-1}.

X-Ray photoelectron spectroscopy (XPS) was carried out using a ThermoFisher ESCALAB Xi+ instrument with a monochromatic Al Kα X-ray source. The instrument binding energy scale was calibrated to give a binding energy at 932.6 eV for Cu $2p_{3/2}$ line of freshly etched metallic copper. The charge compensation system was used, with the surface of the sample irradiated with a flood of electrons to produce a nearly neutral surface charge. The spectra were recorded by using an X-ray beam of size 650 × 10 microns, a pass energy of 20 eV and a step size of 0.1 eV.

Electrochemical characterization. Electrochemical measurements were performed on an Autolab PGSTAT302N potentiostat

The cyclic voltammetry (CV) for each redox mediator electrode was performed in a typical three-electrode cell, using WO_3 or $Ni(OH)_2$ as the working electrode, the 2 mm Pt rod (Metrohm AG) as the auxiliary electrode and the Ag/AgCl 3 M KCl electrode as the reference electrode. The aqueous solutions of H_2SO_4 (0.5 M) and KOH (1 M) were used for the acidic and alkaline cell, respectively.

Chronopotentiometry of the assembled amphoteric decoupled water electrolysis cell was performed by applying 10 mA current between the Pt working electrodes and 100 mA in the case of auxiliary electrodes on carbon cloth. The threshold voltage for the unfavourable cycle was set to −3.5 V and −3.2 V, and for the favourable cycle to 1 V and 2 V for 10 mA and 100 mA, respectively.

Gas quantitative and qualitative analysis experiments

Gas purity from each cell was analysed by mass spectrometry (MS) using an RGA-100 residual gas analyser (Stanford Research Systems). Prior to MS analysis, the cell was purged with argon. An overpressure of 200 mbar was set, and a blank measurement was performed. The cell was operated at 10 or 100 mA with the same threshold potential as defined in chronopotentiometry measurements above. The blank measurement spectrum was subtracted from the gas sample before analysis. To determine the current efficiency (Faraday efficiency), the volume of hydrogen, produced during the favourable and unfavourable cycle, was determined. The volume measurement of the produced hydrogen was carried out by the volumetric displacement method. Hydrogen volume was measured in an acid cell during a favourable cycle and in an alkaline cell during an unfavourable cycle. A glass capillary with an inner diameter of 1 mm was used as a displacement volume.

Author contributions

Martins Vanags came up with the concept, performed materials synthesis, prepared electrodes, performed electrochemistry measurements, interpreted results, and wrote the initial version of the paper. Guntis Kulikovskis designed and constructed a two-chamber cell for gas qualitative and quantitative analyses. Laimonis Jekabsons performed the mass spectrometry measurements and qualitative gas analysis. Anatolijs Sarakovskis performed XPS studies. Krisjanis Smits carried out the electron microscopy studies. Juris Kostjukovs and Liga Bikse did XRD studies and structural analysis. Andris Šutka initiated and coordinated the research, interpreted the results, aided in the drafting of the manuscript, and supervised the project. All authors have reviewed the manuscript and agreed with its contents.

Conflicts of interest

There are no conflicts to declare.

Acknowledgements

This work has been supported by the European Regional Development Fund within the Activity 1.1.1.2 "Post-doctoral Research Aid" of the Specific Aid Objective 1.1.1 "To increase the research and innovative capacity of scientific institutions of Latvia and the ability to attract external financing, investing in

human resources and infrastructure'' of the Operational Programme ''Growth and Employment'' (No. 1.1.1.2/VIAA/3/19/466). Institute of Solid-State Physics, the University of Latvia as the Centre of Excellence has received funding from the European Union's Horizon 2020 Framework Programme H2020-WIDESPREAD-01-2016-2017-TeamingPhase2 under grant agreement no. 739508, project CAMART^2.

Open Access Article. Published on 05 April 2022. Downloaded on 8/20/2025 12:00:37 PM.
This article is licensed under a Creative Commons Attribution 3.0 Unported Licence.

Notes and references

1 I. Mexis and G. Todeschini, *Energies*, 2020, **13**, 3616.
2 M. A. Pellow, C. J. M. Emmott, C. J. Barnhart and S. M. Benson, *Energy Environ. Sci.*, 2015, **8**, 1938–1952.
3 N. Nitta, F. Wu, J. T. Lee and G. Yushin, *Mater. Today*, 2015, **18**, 252–264.
4 A. Eftekhari, *Sustainable Energy Fuels*, 2017, **1**, 2053–2060.
5 Y. Chen, Y. Kang, Y. Zhao, L. Wang, J. Liu, Y. Li, Z. Liang, X. He, X. Li, N. Tavajohi and B. Li, *J. Energy Chem.*, 2021, **59**, 83–99.
6 N. Kirkaldy, G. Chisholm, J. Chen and L. Cronin, *Chem. Sci.*, 2018, **9**, 1621–1626.
7 Q. Zhang, J. Kang and Y. Wang, *ChemCatChem*, 2010, **2**, 1030–1058.
8 Y. N. Regmi, E. Tzanetopoulos, G. Zeng, X. Peng, D. I. Kushner, T. A. Kistler, L. A. Kingand and N. Danilovic, *ACS Catal.*, 2020, **10**, 13125–13135.
9 M. Schalenbach, G. Tjarks, M. Carmo, W. Lueke, M. Mueller and D. Stolten, *J. Electrochem. Soc.*, 2016, **163**, 3197–3208.
10 J. Brauns and T. Turek, *Processes*, 2020, **8**, 248.
11 F. Yu, H. Zhou, Y. Huang, J. Sun, F. Qin, J. Bao, W. A. Goddard, S. Chen and Z. Ren, *Nat. Commun.*, 2018, **9**, 2551.
12 R. L. LeRoy, C. T. Bowen and D. J. LeRoy, *J. Electrochem. Soc.*, 1980, **127**, 1954.
13 Q. Lei, B. Wang, P. Wang and S. Liu, *J. Energy Chem.*, 2019, **38**, 162–169.
14 Y. Li, J. Chen, P. Cai and Z. Wen, *J. Mater. Chem. A*, 2018, **6**, 4948–4954.
15 J. Xu, I. Amorim, Y. Li, J. Li, Z. Yu, B. Zhang, A. Araujo, N. Zhang and L. Liu, *Carbon Energy*, 2020, **2**, 646–655.
16 J. Huang, Y. Xie, L. Yan, B. Wang, T. Kong, X. Dong, Y. Wang and Y. Xia, *Energy Environ. Sci.*, 2021, **14**, 883–889.
17 M. D. Symes and L. Cronin, *Nat. Chem.*, 2013, **5**, 403–409.
18 B. Rausch, M. D. Symes and L. Cronin, *J. Am. Chem. Soc.*, 2013, **135**, 13656–13659.
19 B. Rausch, M. D. Symes, G. Chisholm and L. Cronin, *Science*, 2014, **345**, 6202.
20 L. G. Bloor, R. Solarska, K. Bienkowski, P. J. Kulesza, J. Augustynski, M. D. Symes and L. Cronin, *J. Am. Chem. Soc.*, 2016, **138**, 6707–6710.
21 B. You and Y. Sun, *Acc. Chem. Res.*, 2018, **51**, 1571–1580.
22 A. Landman, H. Dotan, G. E. Shter, M. Wullenkord, A. Houaijia, A. Maljusch, G. S. Grader and A. Rothschild, *Nat. Mater.*, 2017, **16**, 646–651.
23 W. Pu, Z. Song, J. Yan, H. Xu, H. Ji, S. Yuan and H. Li, *J. Mater. Sci.*, 2019, **54**, 12463–12475.
24 M. C. Biesinger, B. P. Payne, L. W. M. Lau and A. Gerson, *Surf. Interface Anal.*, 2009, **41**, 324–332.
25 B. Ash, V. S. Nalajala, A. K. Popuri, T. Subbaiah and M. Minakshi, *Nanomaterials*, 2020, **10**, 1878.
26 R. Barnard, C. F. Randell and F. L. Tye, *J. Appl. Electrochem.*, 1980, **10**, 127–141.
27 M. M. Mohamed, T. M. Salama, M. A. Hegazy, R. M. Abou Shahba and S. H. Mohamed, *Int. J. Hydrogen Energy*, 2019, **44**, 4724–4736.
28 J. E. Benson, H. W. Hohn and M. Boudart, *J. Catal.*, 1966, **5**, 307–313.

 This journal is © The Royal Society of Chemistry 2022